Received: 14 July 2020 | Revised: 7 September 2020 | Accepted: 8 September 2020

DOI: 10.1111/jace.17490

Journal of the American Ceramic Society

ORIGINAL ARTICLE

Microstructure and mechanical behavior of TiO_2-MnO-doped alumina/alumina laminates

Marcelo Daniel Barros[1,2] | **Hans Jelitto**[2] | **Dachamir Hotza**[1] | **Rolf Janssen**[2]

[1]Graduate Program in Materials Science and Engineering (PGMAT), Laboratory of Processing of Ceramics (PROCER), Federal University of Santa Catarina (UFSC), Florianópolis, SC, Brazil

[2]Institute of Advanced Ceramics, Hamburg University of Technology (TUHH), Hamburg, Germany

Correspondence
Rolf Janssen, Institute of Advanced Ceramics, Hamburg University of Technology (TUHH), 21073 Hamburg, Germany.
Email: janssen@tuhh.de

Abstract

Tapes of TiO_2-MnO-doped alumina (d-Al_2O_3) and pure alumina (Al_2O_3) were shaped via tape casting. Laminates with three different layer numbers and respective thicknesses were produced and sintered at 1200°C. The microstructure and mechanical behavior of laminates were investigated and compared to the respective monolithic references (d-Al_2O_3 and Al_2O_3). The use of dopants in alumina decreased the initial sintering temperature, leading to higher densification at 1200°C (~98% theoretical density (TD)) when compared to Al_2O_3 (~73% TD). The higher density was reflected in a higher Young's modulus and hardness for doped alumina. A region of diffusion of dopants in pure alumina layers was observed along the interface with doped layers. The mechanical strength of d-Al_2O_3 samples sintered at 1200°C was not statistically different from Al_2O_3 samples sintered at 1350°C. The strength of laminates composed of doped layers with undoped, porous interlayers did not change. Nevertheless, as the thickness of these porous interlayers increases, a loss of strength was observed. Monolithic references showed constant values of fracture toughness (K_{IC}), ~2 MPa·$m^{1/2}$, and linear crack path. On the other hand, K_{IC} of laminates increases when the crack propagates from weak Al_2O_3 layers to dense d-Al_2O_3 layers.

KEYWORDS

alumina laminates, laminate design, mechanical strength, R-curve

1 | INTRODUCTION

Since Clegg et al[1] were successful in producing weak interfaces in laminated ceramic composites to obtain a non-catastrophic failure, several studies were done presenting ceramics with laminar structures as an effective alternative to overcome the typical brittleness of monolithic ceramics, to avoid catastrophic failure, to modify the crack path, and to increase fracture toughness.

One approach widely used for ceramic laminates is to generate compressive residual stresses in layers due to different coefficients of thermal expansion (CTE), considering interfaces with strong adhesion. The idea is to achieve high levels of compressive stresses in these layers to control or oppose crack propagation, activating toughening mechanisms as crack arresting, crack bifurcation, and microcracking. Thus, it is possible for laminates to enhance fracture toughness and to absorb more energy during failure, compared to reference monolithic ceramics.[2-11].

Another way to enhance toughness in laminates is to produce weak interfaces or layers to cause crack deflection. This behavior strongly depends on the fracture energy and Young's modulus of weak and strong layers of the composite. The volume fraction of pores and the pore interaction have an important contribution to ensure that crack continues

propagating in the weak layer or interface. The porosity in these materials is normally produced by introducing fugitive pore former agents, such as starch, graphite, or polymers.[12-18]

On the other hand, tailoring the sinterability of a ceramic laminate in both strong and weak layers is possible by using starting powders with different particle sizes or dopants to reduce sintering temperatures.[19] The sintering driving force is inversely proportional to the particle size. The finer the particles, the faster the sintering rate. Thus, sintering for smaller particles occurs at lower temperatures, due to the smaller diffusion distances. There is also a relationship with melting temperature, which decreases with lower particle sizes.[20,21]

The use of sintering aids as titanium and manganese oxides has been proved effective to lower alumina sintering temperature and to promote crystal growth. Winkler et al[22] have used TiO_2 as a sintering aid and grain growth promoter for alumina. Jones, Cutler and co-authors[23,24] added a total of 4 wt% manganese and titanium oxides or copper and titanium oxides, and the result was an effective reduction in the sintering temperature to the range of 1300 to 1400°C. Kostić et al[25] achieved ~95% theoretical density (TD) after sintering alumina at 1300°C with 5 wt% of a TiO_2/MnO mix, contrasting with 58% TD obtained for pure alumina submitted to the same heat treatment. Xue and Chen[26] used a colloidal process for alumina with 0.9 mol% CuO + 0.9 mol% TiO_2 + 0.1 mol% MgO + 0.1 mol% B_2O_3. As a result, they sintered alumina at 1070°C for 1 hour and obtained 99.3% TD. Sathiyakumar and Gnanam[27] also used colloidal processing with MnO and TiO_2 as sintering additives. The authors reduced the sintering temperature from 1550°C to 1200°C-1250°C, reaching 99.2%–99.6% TD.

One of the most used methods to obtain reliable results of fracture toughness as a function of crack length in ceramics composites is the Single Edge "V" Notch Beam (SEVNB) technique.[28,29] A device developed by Jelitto et al[30] uses the SEVNB method in a very stiff apparatus that allows the crack to stably grow. By performing several loading-unloading cycles, many values of fracture toughness at different crack lengths can be obtained with one single specimen.[10,30-32]

In this work, alumina-based laminates were produced by tape casting with tailored weak interlayers created via partial sintering. Nondoped alumina is supposed to produce less dense, weaker layers than the TiO_2-MnO-doped dense layers, enhancing fracture toughness and creating a particular R-curve behavior. Microstructure, mechanical behavior, and crack propagation were characterized and correlated with the laminate configurations.

2 | MATERIALS AND METHODS

Two different starting powders were chosen to produce the ceramic laminates. The first powder is the high-purity submicrometric alumina powder Taimicron TM-DAR (Al_2O_3, Taimei Chemicals, Japan), with an average particle size as received of 150 nm. The second powder is a mixture of the Taimicron TM-DAR with 1.68 wt% titanium dioxide (TiO_2, Kemira, Finland) and 2.32 wt% manganese oxide (MnO_2, Sigma-Aldrich, Germany). This mixture was produced utilizing high-energy ball milling and achieved a final average particle size of 220 nm.

TABLE 1 Slurry formulation for the production of alumina and doped alumina tapes

Component	Quantity
Powder (solids)	21 vol%
Deionized water (liquid)	79 vol%
Additives (referred to solids content)	
Mowilith LDM 6138	30.0 wt%
Darvan C-N	2.0 wt%
NINOL PK-80 BR	1.5 wt%
Antifoam Y-30	1.0 wt%

Ceramic slurries for tape casting of each of these powders were produced using 21 vol% solid loading. In the first step, the powder was deagglomerated in deionized water with the addition of a dispersing agent (Darvan C-N, Vanderbilt Minerals, USA) using ball milling for 4 hours. Then, a binding agent (Mowilith LDM 6138, Celanese, USA), a nonionic surfactant (Ninol PK-80 BR, Stepan, USA), and an antifoamer (Antifoam Y-30, Sigma-Aldrich, Germany) were added and ball-milled for more 30 minutes. Slurries were placed in an ultrasonic bath for 5 minutes and let to rest for 1 hour to ensure the removal of bubbles. The slurry formulation is presented in Table 1.

Tapes were cast onto a silicone-coated tape (Mylar®) at a casting speed of 6 cm/min using a tabletop tape caster (CC-1200, Tape Casting Warehouse, USA) and subsequently dried at room temperature for 24 hours. The lamination of samples was performed in a warm press at 20 MPa and 65°C for 5 minutes. Three different configurations of composites were produced for structures with weak layers. Laminates of doped and pure alumina were stacked in an ordered sequence, resulting in different layer thickness ratios. Additionally, green laminates of monolithic pure alumina and doped alumina were manufactured as reference materials. Green tapes were laminated in order to achieve the approximate dimensions of $3.5 \times 15 \times 50\ mm^3$ after sintering. Figure 1 and Table 2 present the produced samples and their respective structure.

The burn out of organics was performed with a heating rate of 0.3°C/min until 600°C and a holding time of 1 hour. All samples have been sintered at 1200°C. Additionally, pure alumina samples were sintered as well at 1350°C. The higher sintering temperature was used for pure alumina to ensure rigid well-sintered samples and to compare with doped alumina sintered at lower temperatures. In both heat treatments, a heating rate of 5°C/min and a holding time of 2 hours were used. The cooling rate was set to 10°C/min.

The density of monolithic sintered samples was measured with the Archimedes method, in an analytical balance (ABT

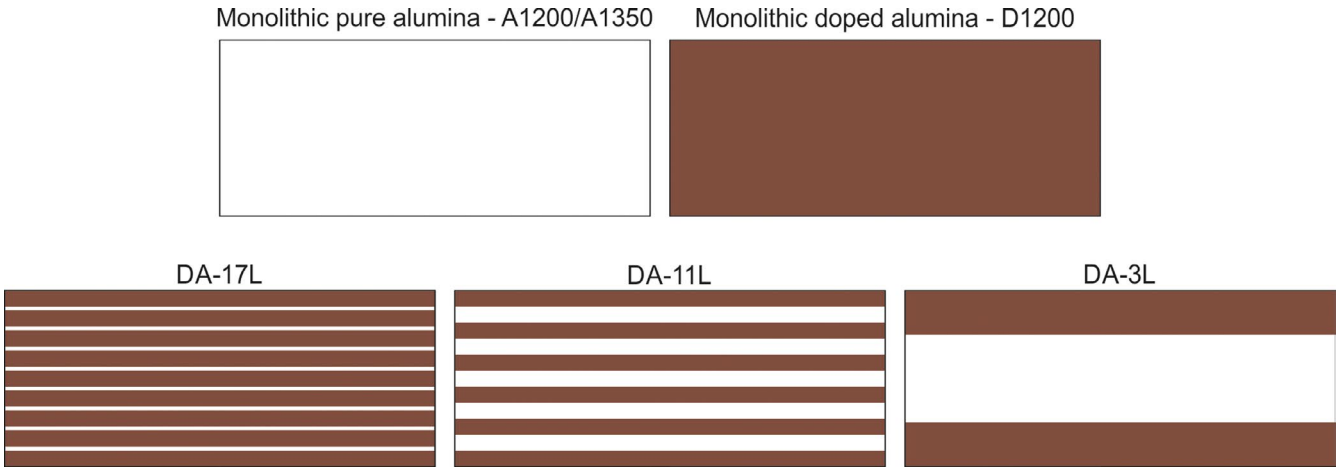

FIGURE 1 Illustration of the samples produced in this work: A1200/A1350; D 1200; DA-17L; DA-11L; DA-3L. White is pure alumina and brown is doped alumina [Color figure can be viewed at wileyonlinelibrary.com]

TABLE 2 Characteristics of monolithic reference and composites materials

Sample name	Material	Number of tapes in each layer	Number of layers	Layer thickness ratio (d-Al_2O_3:Al_2O_3)	Sintering temperature (°C)
A1200	Monolithic pure alumina	Al_2O_3: 44	—	—	1200
A1350	Monolithic pure alumina	Al_2O_3: 44	—	—	1350
D1200	Monolithic doped alumina	d-Al_2O_3: 44	—	—	1200
DA-17L	Doped and pure alumina layers	d-Al_2O_3: 4 Al_2O_3: 1	d-Al_2O_3: 9 Al_2O_3: 8	4:1	1200
DA-11L	Doped and pure alumina layers	d-Al_2O_3: 4 Al_2O_3: 4	d-Al_2O_3: 6 Al_2O_3: 5	1:1	1200
DA-3L	Doped and pure alumina layers	d-Al_2O_3: 11 Al_2O_3: 22	d-Al_2O_3: 2 Al_2O_3: 1	1:2	1200

100-5NM, Kern, Germany). Linear shrinkage of monolithic samples was investigated as a function of temperature, analyzed by dilatometry (DIL 402 PC, Netzsch, Germany). Residual stresses were measured according to Equations 1 and 2 from Chartier et al[33]

$$\sigma_{Al_2O_3} = \Delta\varepsilon \cdot E'_{Al_2O_3} \cdot \left(1 + \frac{t_{Al_2O_3} \cdot E'_{Al_2O_3} \cdot n_{Al_2O_3}}{t_{d-Al_2O_3} \cdot E'_{d-Al_2O_3} \cdot n_{d-Al_2O_3}}\right)^{-1} \quad (1)$$

$$\sigma_{d-Al_2O_3} = \Delta\varepsilon \cdot E'_{d-Al_2O_3} \cdot \left(1 + \frac{t_{d-Al_2O_3} \cdot E'_{d-Al_2O_3} \cdot n_{d-Al_2O_3}}{t_{Al_2O_3} \cdot E'_{Al_2O_3} \cdot n_{Al_2O_3}}\right)^{-1} \quad (2)$$

where $\Delta\varepsilon$ is the difference in thermal strain between adjacent layers; $E' = \frac{E}{1-\nu}$ being E is the elastic modulus and ν is the Poisson's ratio; t is the mean thickness of layers; and n is the number of layers. Alumina Poisson's ratio of 0.22 was used for both samples. The other parameters were experimentally measured.

A nanoindenter (G200, Agilent Technologies, USA) equipped with a Berkovich tip was used to measure the elastic modulus and hardness of monolithic sintered samples. At least 25 indentations were performed for each measurement by using the Continuous Stiffness Measurement (CSM) technique.[34] Indentations were also done along the interfaces in order to analyze the interaction between doped and pure alumina layers in the composites. The advance and lateral displacement related to the last indentation were 5 and 60 μm, respectively.

Microstructure and fracture analyses were conducted using an optical microscope (OM, BX51, Olympus, Germany) and a scanning electron microscope (SEM, Supra VP 55, Zeiss, Germany). Microstructure was revealed by means of thermal etching at 90% of the sintering temperature for 30 minutes. The grain size was measured using the line-intercept method with the help of an image analysis software (Lince 2.4.2e, Ceramics Group, TU Darmstadt, Germany) using 300 grain measures per sample.

Four-point bending tests were performed using as-sintered prismatic bars (3.5 × 2.5 × 25 mm^3) cut from the laminates

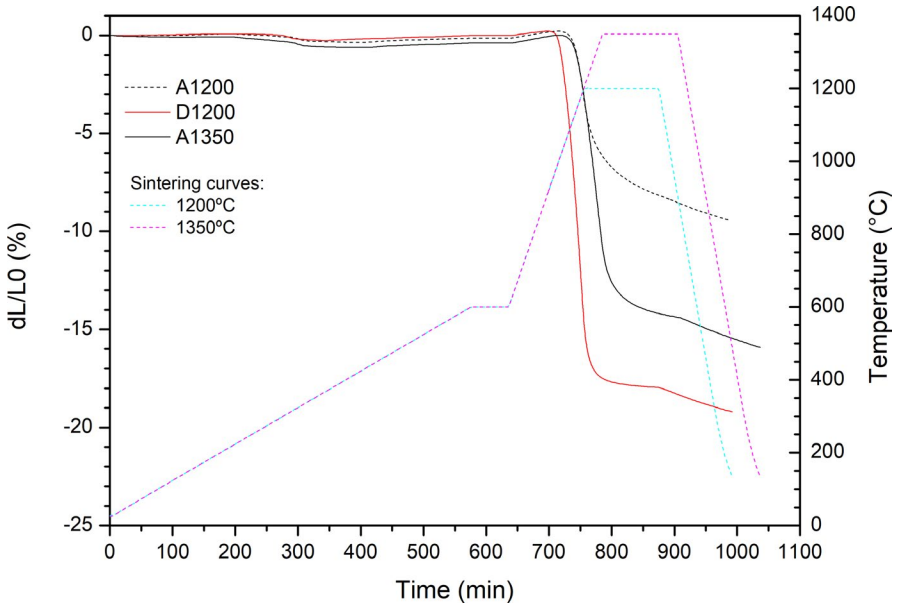

FIGURE 2 Dilatometric analyses of A1200, D1200, and A1350 monolithic reference samples [Color figure can be viewed at wileyonlinelibrary.com]

using a universal test machine (Series 1605B, ATS, USA). Outer and inner spans had a distance of 20 and 10 mm, respectively. A loading speed of 1 mm/min was applied. At least 10 samples of each material were tested.

For the R-curve tests, prismatic bars ($3.5 \times 2.5 \times 50$ mm^3) were notched with a diamond disc saw until achieving 45%–50% of the initial height. The notches were sharpened using an automated razor blade device and diamond paste to avoid a finite notch radius effect during the test.[31] R-curve tests were performed according to Single Edge V-notched Beam (SEVNB) stable crack growth configuration in a very stiff displacement-controlled house-made device.[35] The distances between the outer (s_1) and inner (s_2) rollers were 40 and 20 mm, respectively. A loading speed of 0.0012 mm/min was applied. Thereby, stable crack growth was achieved by partial unloading and reloading cycles. As soon as the crack started to propagate, the sample was partially unloaded by an automatic computer-controlled process based on the continuous evaluation of the slope in the load-displacement diagram. The crack length was determined with the compliance method. Two position encoders (displacement sensor WI/2mm-T, HBM, Hannover, Germany) were used, one placed at the center of the sample and the other one, 15 mm aside. By considering the difference of both displacement signals during partial unloading, the pure bending compliance could be calculated without the necessary correction due to the machine compliance. The equations are used on the basis of beam theory, as described in detail by Fett and Diegele,[36] exactly for the geometry of the given load cell. Thus, force and crack length were recorded at each cycle to determine fracture toughness (K_{IC}). For SEVNB 4-point bending tests, Equations 3 and 4 were used[37]

:

$$K_{\mathrm{IC}} = \frac{3F \cdot \Delta s \cdot \sqrt{l} \cdot \Gamma(\alpha)}{2bh^{3/2}(1-\alpha)^{3/2}} \tag{3}$$

with

$$\Gamma(\alpha) = 1.1215\sqrt{\pi}\left[\frac{5}{8} - \frac{5}{12}\alpha + \frac{1}{8}\alpha^2 + 5\alpha^2(1-\alpha)^6 + \frac{3}{8}e^{\left(-6.1342\frac{\alpha}{(1-\alpha)}\right)}\right], \quad \alpha = \frac{l}{h} \text{ and } \Delta s = s_1 - s_2 \tag{4}$$

where F is the applied force on the specimen in each loading cycle; l is the crack length; b and h are the width and height of the specimen, respectively; α is the relative crack length, and $\Gamma(\alpha)$ is a geometric factor. The work of fracture (W_F) was calculated by dividing the area under the load-displacement curves by twice the area of the unnotched parts of samples.

3 | RESULTS AND DISCUSSION

Doping by MnO and TiO_2 effectively enhanced the sinterability of Al_2O_3 as compared by dilatometry analysis of monolithic reference samples (Figure 2). Shrinkage starts around 910°C for doped alumina and 1000°C for pure alumina samples. A1200 and D1200 achieved a final shrinkage of 9.5% and 19.2%, respectively, while A1350 obtained 15.9%. The CTE (α) measured was 11.8×10^{-6}/K for A1200, 11.4×10^{-6}/K for D1200, and 12.4×10^{-6}/K for A1350.

Figure 3 shows the microstructure of the monolithic reference samples after sintering. The measured relative density of samples is 72.9 ± 1.5% for A1200, 97.8 ± 0.4% for D1200, and 90.3 ± 1.3% for A1350. The average grain size of A1200, D1200, and A1350 were determined as 301 ± 126 nm, 448 ± 230 nm, and 323 ± 154 nm, respectively. As expected, A1200 presents higher porosity and lower average grain size and dispersion of sizes compared to A1350. D1200 presents higher densification and enhanced grain growth compared to both pure alumina samples, for example, sintered at 1200°C

and 1350°C. Enhancement in sintering is related to grain boundaries and volume diffusions and the presence of anion and cation vacancies.[24,38-40]

The mechanical properties, particularly Young's modulus and hardness (Table 3), exhibited the well-known dependency on porosity, for example, higher values for the more dense samples.[41] Figure 4 shows the tested samples to give a better idea of how the samples look like after sintering. Table 4 presents the final average thickness of each layer in the sintered composites and the ratios between them. It was observed that the values of the final ratio were not in accordance with the ones established in methodology, and this is directly linked to the processing of samples (eg, differences in tapes' thickness and lamination process). However, different final ratios for each type of composite were achieved as intended. The estimated relative density of composites measured using monolithic reference densities and average layer thickness is 95.1% for DA-17L, 89.2% for DA-11L, and 86.0% for DA-3L.

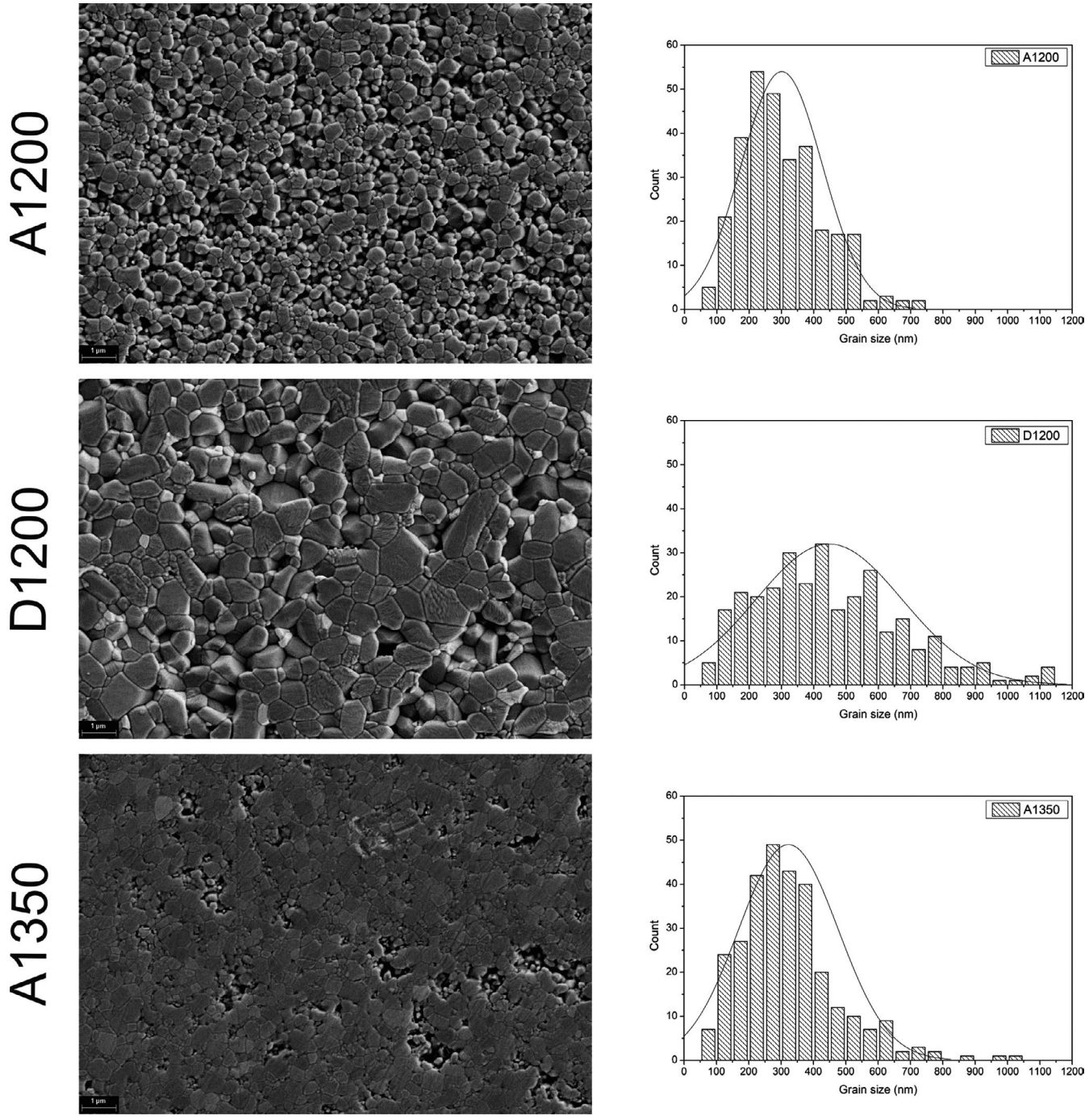

FIGURE 3 Microstructure of monolithic reference samples after sintering (left) and histograms (right) of grain size distribution

Figure 5 shows the OM and SEM micrographs of DA-17L at low (left hand) and high magnification, the later one focusing on the interface between doped and pure alumina.

TABLE 3 Values of hardness and elastic modulus of monolithic reference samples

Sample	Berkovich hardness (GPa)	E (GPa)
A1200	11 ± 1	236 ± 7
D1200	18 ± 2	352 ± 29
A1350	17 ± 2	303 ± 21

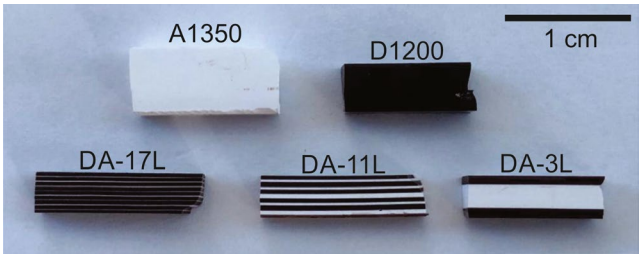

FIGURE 4 Samples of monolithic references A1350 and D1200, and composites DA-17L, DA-11L, and DA-3L produced in this work [Color figure can be viewed at wileyonlinelibrary.com]

TABLE 4 Average layer thickness of pure and doped alumina in each composite, and the layer thickness ratio obtained after sintering

Sample	Layer d-Al_2O_3 (μm)	Layer Al_2O_3 (μm)	Final ratio (d-Al_2O_3:Al_2O_3)
DA-17L	353 ± 31	49 ± 11	7.1:1
DA-11L	400 ± 48	253 ± 91	1.6:1
DA-3L	910 ± 86	1640 ± 301	1:1.8

In the optical image, a color gain between doped and pure layers is obvious. The shift from brownish (in the doped layer) to yellowish-white (in the pure alumina layer) is almost continuous rather than discrete, indicating diffusion of the dopants. The thickness of this region could be optically estimated to be 51 ± 7 μm, which is in agreement with the gradual change of elasticity and hardness across the interface as measured by nanoindentation (~50 μm, see Figure 6).

Table 5 lists the average maximum strength (σ_f). According to the two-tailed *t* tests with 95% confidence interval applied for the comparison between all the samples, five combinations are significantly different, that is, presented p-value (significance level) lower than 0.05: A1350 with DA-11L, D1200 with DA-11L and DA-3L, and DA-17L with DA-11L and DA-3L. It is interesting to notice that the obtained p-value for the comparison between A1350 and DA-3L was 0.052, which is very near to the threshold to consider them significantly different.

The use of dopants to reduce the sintering temperature of alumina was successfully applied without losing the mechanical strength. Doped alumina samples presented larger grains, but also higher density, thereby compensating their effect on mechanical strength.[42] It is also interesting to note that with the thinnest weak layers (DA-17L), there is no loss in the mechanical strength compared to the references. Nevertheless, the values of σ_f decreased around 14% for DA-11L and DA-3L, when compared to monolithic samples and DA-17L, indicating a slight weakening of samples with increasing thickness of weak layers.

Figure 7 shows the representative load-displacement curves obtained during R-curve measurements, corrected as done before in other works with the same device.[30,43]

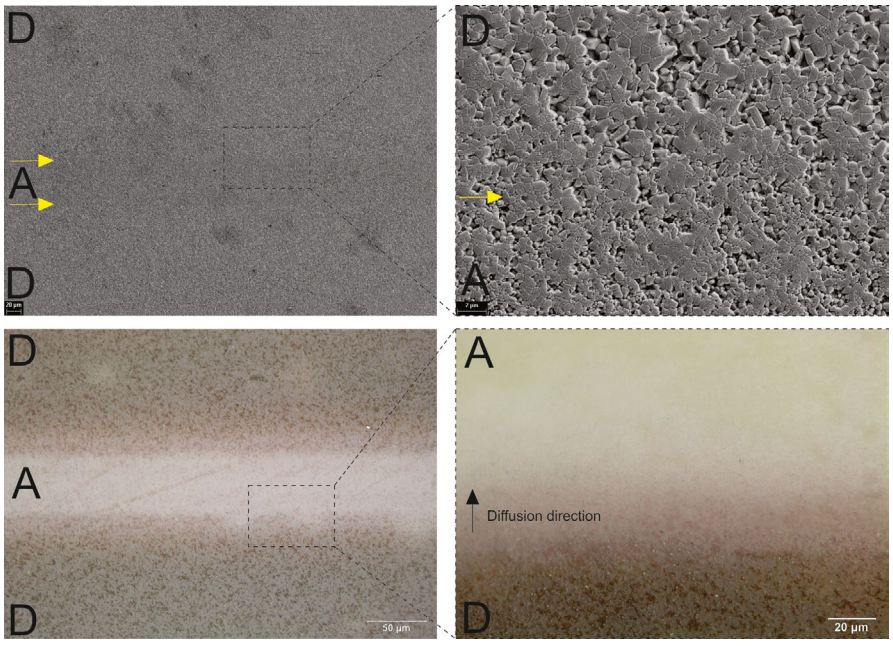

FIGURE 5 SEM (upper part) and OM (lower part) of the DA-17L sample. A and D stand for pure (Al_2O_3) and doped (d-Al_2O_3) alumina layers in the composite. Horizontal arrows indicate the location of the interface between doped and pure alumina. The vertical arrow shows the diffusion direction of the dopants through the pure alumina layer [Color figure can be viewed at wileyonlinelibrary.com]

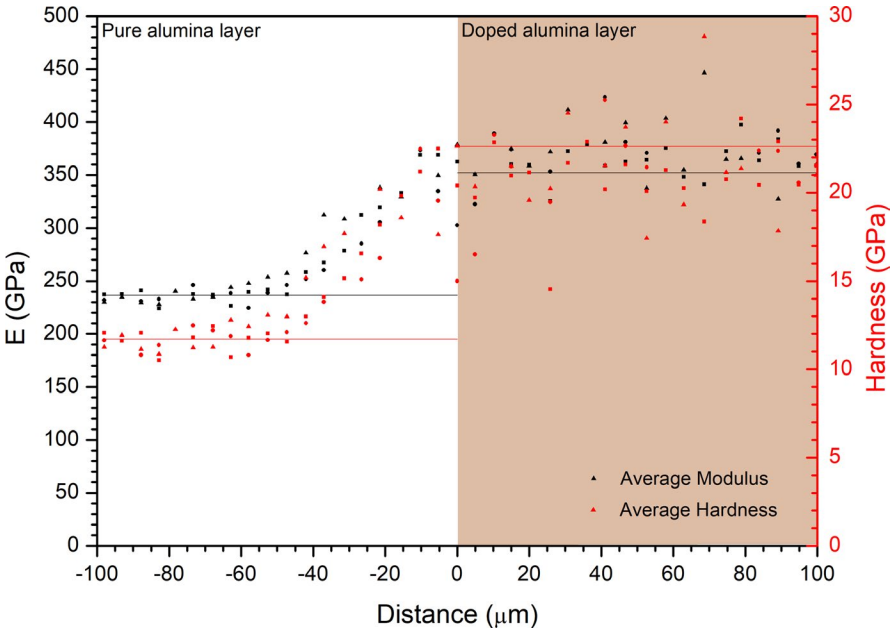

FIGURE 6 Young's modulus (left black Y-axis) and hardness (right red Y-axis) obtained by nanoindentation across the interface region. The diffusion region was estimated by the increment of hardness and elasticity from pure to doped alumina. The reference average modulus (black straight line) and hardness (red straight line) are presented in the graphic [Color figure can be viewed at wileyonlinelibrary.com]

TABLE 5 Average maximum strength (σ_f) of tested samples in 4-point bending

Sample	Samples tested	σ_f (MPa)
A1350	10	258 ± 26
D1200	11	266 ± 33
DA-17L	19	268 ± 27
DA-11L	10	223 ± 24
DA-3L	13	232 ± 35

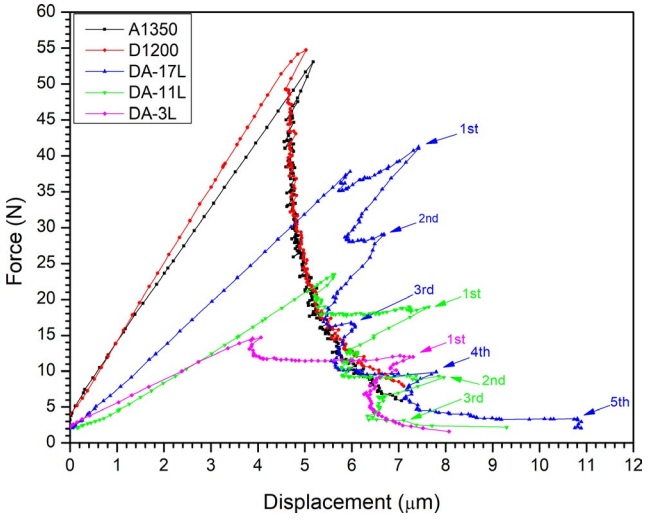

FIGURE 7 Load-displacement curve of R-curve measurement for alumina, doped alumina, and DA composites. Monolithic samples presented, in general, a continuous decreasing curve as shown for A1350 and D1200. Meanwhile, the curves for composites presented a stepwise behavior. Arrows indicate the rising step load regions caused by crack propagation through interfacial zones [Color figure can be viewed at wileyonlinelibrary.com]

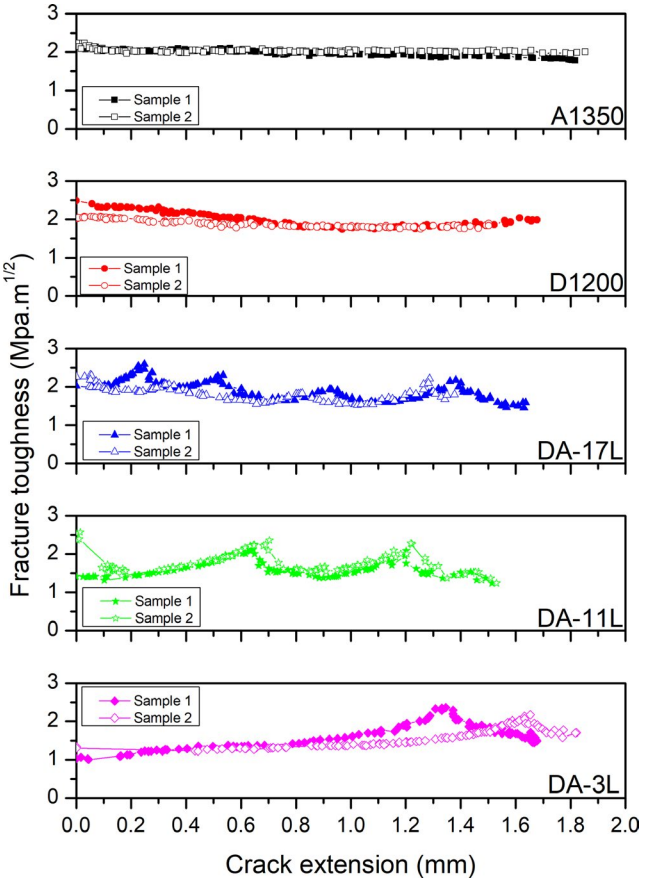

FIGURE 8 R-curve of monolithic reference and composite samples. For each type, two samples were tested [Color figure can be viewed at wileyonlinelibrary.com]

This procedure was adopted because due to the dead weight of the machine's upper support, the force did not start at zero. Each dot represents the maximum force of

TABLE 6 Values of average, work of fracture, K_{IC} maximum, average K_{IC} minimum, and the average difference

Sample	W_F (Jm^{-2})	K_{IC} min. ($MPa{\cdot}m^{1/2}$)	K_{IC} max. ($MPa{\cdot}m^{1/2}$)	$K_{IC\,Max} - K_{IC\,Min}$ ($MPa{\cdot}m^{1/2}$)
DA-17L	7.5 ± 0.3	1.7 ± 0.2	2.1 ± 0.2	0.4 ± 0.1
DA-11L	6.5 ± 0.6	1.3 ± 0.1	2.2 ± 0.2	0.8 ± 0.1
DA-3L	5.1 ± 0.7	1.3 ± 0.2	2.2 ± 0.1	1.3 ± 0.1

each cycle. Monolithic samples (black and red lines) present the typical behavior of materials that have a nearly constant K_{IC}. In these materials, cycle by cycle, displacement increases slightly as force decreases, according to the reduction of the sample cross-section (disregarding statistical scattering).

The composites exhibit different behavior. The force increases until the crack starts to propagate, then it goes down similarly to monolithic references with a constant toughness regime. As the crack propagates in the porous region, it comes closer to the interface (which has residual stress fields) and approaches the next doped alumina dense region. Then, an increase in the force is necessary to drive the crack due to the mismatch of fracture energy. After entering the dense layer, the maximum forces at each cycle drop again until the next interfacial zone. The thicker the alumina layers, the higher the reinforcement effects. This is not likely caused by a size effect on reinforcement efficiency, for example, the reinforcement effects should be large if both compressive and tensile layers have similar or the same added layer thicknesses, such as DA-11L and DA-3L. Otherwise, the thick layers would dominate and the thin layers have less influence, which reduces the effect. Even avoided during sample preparation, still a small effect of the finite notch root radius[30] was observed in some cases (eg, D1200 in Figure 7).

Figure 8 shows the results of fracture toughness as a function of the crack extension (measured right after the initial notch length). Mean fracture toughness and work of fracture obtained were, respectively, 2.0 ± 0.1 $MPa{\cdot}m^{1/2}$ and 7.3 ± 0.7 Jm^{-2} for A1350, and 1.9 ± 0.2 $MPa{\cdot}m^{1/2}$ and 8.4 ± 1.4 Jm^{-2} for D1200. A nearly constant R-curve behavior is observed, which is typical for monolithic alumina.[10] K_{IC} is not significantly different; however, higher work of fracture is observed for D1200 due to higher densification and the influence of large grains, which results in a larger crack surface.[19]

Different R-curve behavior is observed for composites. An increase of crack resistance was observed when the crack reaches the interface zone, following the behavior observed in force-displacement curves. When the rising plateau steps of force occur, fracture toughness increases until reaching a maximum. After that, the force decreases due to propagation in dense layers, and fracture resistance decreases together with it until reaching a minimum. This cycle repeats every time the crack approaches the weak pure dense doped alumina interface. The thicker the alumina layers are, the slighter is the increase in K_{IC}. The R-curves of the samples DA-17L exhibit four local maxima, when the crack passes through the corresponding four interfaces to the next doped alumina layer. The R-curves of the DA-3L beams have only one maximum, because the crack starts in the middle of the sample and reaches only one interface. Due to the computer-controlled stable crack advance, the data points are relatively close together with low statistical scattering. Table 6 shows the work of fracture, the average maximum and minimum values of fracture toughness for each composite (two samples), K_{ICmax}

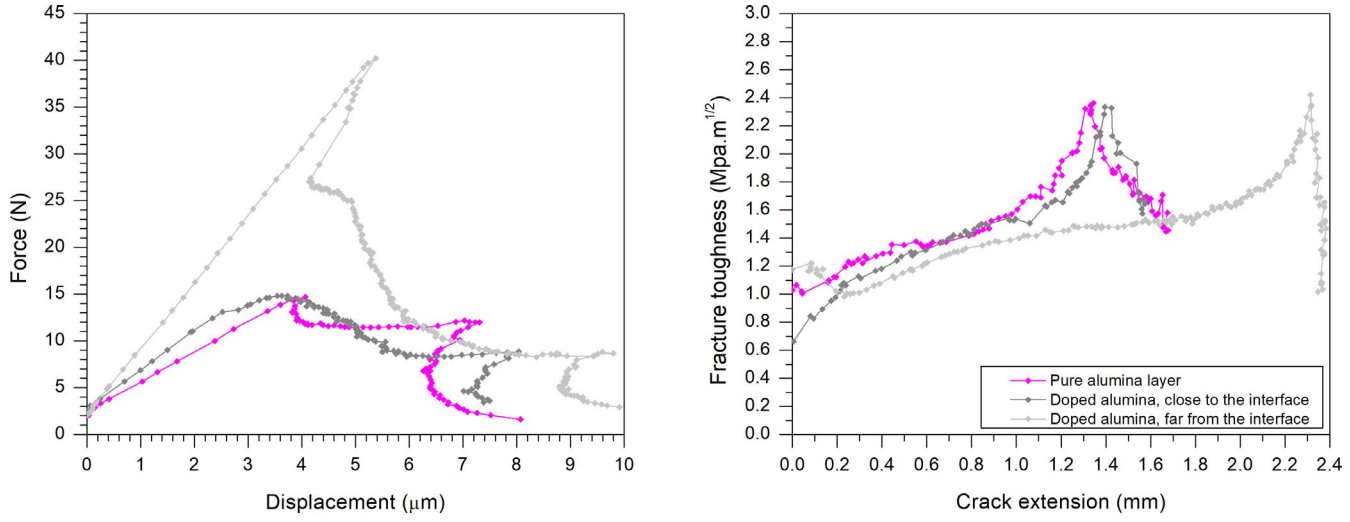

FIGURE 9 Load-displacement (left) and R-curve (right) for samples of DA-3L tested with different notch lengths, so that the crack tip was in different positions: in the middle of the weak pure alumina layer and the first doped alumina layer (far and next to the interface) [Color figure can be viewed at wileyonlinelibrary.com]

TABLE 7 Values of residual stresses calculated by Equations 1 and 2 in layers of composites DA-17L, DA-11L, and DA-3L. The negative signal is referred to compressive stresses, while the positive signal to tensile stresses

	Residual stresses (MPa)	
Sample	**Layer d-Al_2O_3**	**Layer Al_2O_3**
DA-17L	−20	163
DA-11L	−68	129
DA-3L	−97	108

and K_{ICmin}, respectively, and the average difference K_{ICmax} - K_{ICmin} for each sample in each type of composite.

By comparing these values with those obtained for monolithic samples, it is observed that the minimum fracture toughness of composites is lower, but the maximum K_{IC} is higher. Furthermore, the thicker the pure alumina layers in composites, the higher the difference in the minimum and maximum values of fracture toughness. Thus, the alterations of fracture resistance during crack propagation can be tailored by the ratio between the layers d-Al_2O_3:Al_2O_3. The work of fracture reduces with the introduction of weak pure alumina layers, inversely proportional to the thickness of Al_2O_3 layers. The higher the volume of pure alumina, the lower the W_F.

To better understand the effect of the interface in composites, two more samples of DA-3L were made with a smaller notch, where the tip stays before the first interface, still in the doped alumina dense layer. One of the samples was notched close to the interface, and the other far from the interface, around 30% and 15% of samples' height, respectively. R-curve results are shown in Figure 9, together with a DA-3L reference sample (DA-3L in Figures 7 and 8 - Sample 1), where the crack starts to propagate in the middle of the weak pure alumina layer.

The sharp (tilted) maximum of the light gray curve (left diagram) stems from an overload, necessary to start the crack from the short notch (far from the interface). The maxima at 7, 8, and 9 μm displacement correspond to the maxima at 1.4 and 2.3 mm crack extension in the right diagram. As the crack starts to propagate in the doped dense layer, the required force to drive the crack goes down as the remaining layer cross-section gets smaller. Also, in this region, the crack moves into the porous layer, which is favored as confirmed considering the ration of fracture energy and elastic mismatch outlined by He and Hutchinson plot (reduction of maximum force), useful to predict if a crack could be deflected or not at the interface between dissimilar elastic materials.[44] Then, the crack comes closer to the interface, from a porous to dense layer, where there is a small stress field. Directly at the interface, the advancing of the crack is hindered by the change of fracture energy, resulting in the observed rising plateau of force and an increase in fracture toughness. After entering the next layer, the crack is again in a dense region and propagates

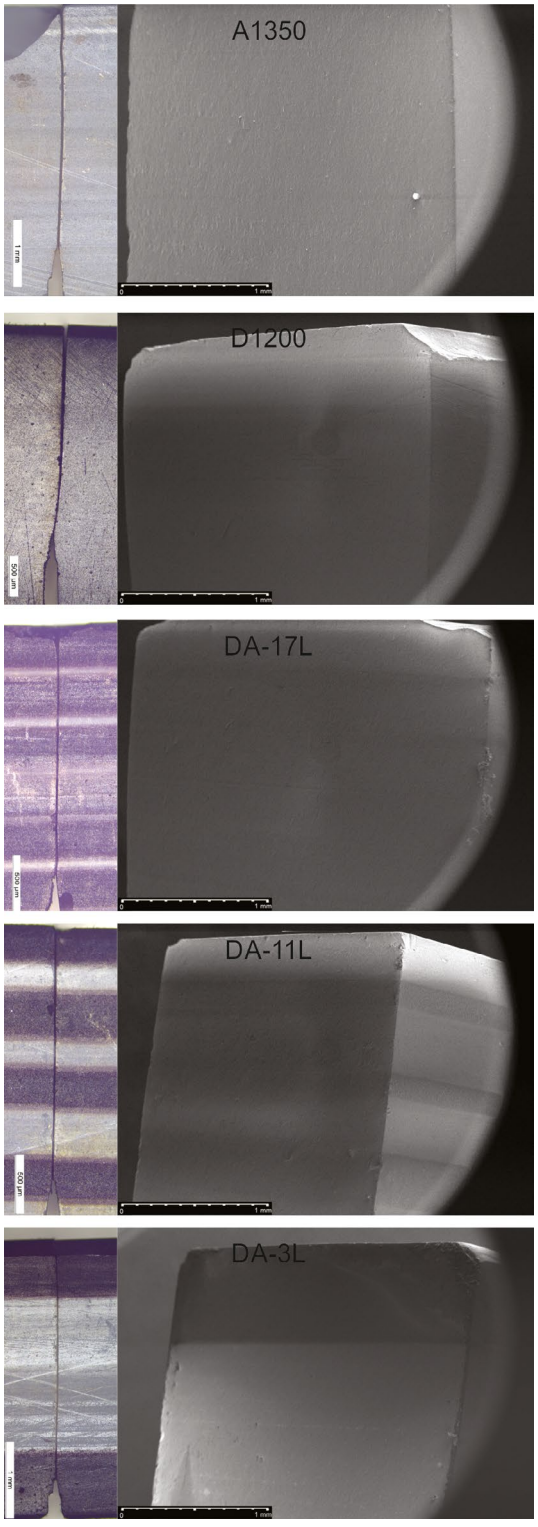

FIGURE 10 Micrographs of fractured samples, OM in the left side, and SEM in the right side. SEM was carried out with an angled sample holder that allows the sample to be with 45° regarding the electron beam [Color figure can be viewed at wileyonlinelibrary.com]

stably until complete failure, similarly to the monolithic references.

Residual stresses also play a role in fracture toughness and crack behavior of composites. The difference between calculated CTE for pure and doped alumina is 0.4×10^{-6}/K, which implies different residual stresses in the layers of each type of composite (see Table 7).

Cooling after sintering developed different degrees of residual stresses. Compressive stresses in d-Al_2O_3 layers might help to improve fracture toughness in these dense layers. On the other hand, tensile stresses in Al_2O_3 layers depreciate crack resistance in these weak layers. Notwithstanding, the magnitude of them is not sufficiently high to modify the crack path (eg, by crack arresting or bifurcation) in compressive layers or to induce unstable crack growth in tensile layers. Another evidence of it is that no edge cracks were observed in these materials.

Investigations of the fractured surfaces of composites (Figure 10) did not reveal visible modifications (eg, crack arrest or deflection) in the crack path. As occurred with the monolithic samples, the crack propagates nearly linearly through the sample, with flat crack faces. Differences in the densification/porosity between layers do not have any influence on the crack path.

4 | CONCLUSIONS

The use of dopants successfully increased the sinterability of alumina and rate of densification, reducing the initial sintering temperature by 90 K and increasing the final shrinkage after sintering at 1200°C. The CTE calculated for doped Al_2O_3, 0.4×10^{-6}/K, was lower than that for pure Al_2O_3 at this sintering temperature. Grain size in doped alumina is higher than that in pure alumina samples.

Young's modulus and hardness of doped Al_2O_3 are higher than those of pure Al_2O_3 due to higher density. In laminates of doped and pure alumina, diffusion of dopants occurs. In the case of sintering at 1200°C, a diffusive region of ~50 μm was detected after cooling to room temperature. Four-point bending tests showed that the mechanical strength of alumina sintered at 1350°C is statistically in the same range as doped alumina sintered at 1200°C, confirming the effectiveness of dopants in reducing the sintering temperature of alumina without substantial changes of mechanical properties.

In layered composites with weak layers of pure, only partially sintered alumina, it was observed that samples with thin weak layers (DA-17L) did not lose strength when compared to the references, unlike samples DA-11L and DA-3L with thicker weak layers that presented a slight decrease in strength. Thus, for thin weak layers, their effect on the strength is negligible. As this thickness increases, a loss in strength must be taken into account.

Monolithic samples presented nearly constant resistance during crack propagation. However, laminates presented an alternation behavior: K_{IC} increases when the crack propagates through the interfacial zones, from weak pure alumina layers to dense doped alumina layers. This reinforcement effect is more evidenced (differences between K_{IC} minimum and maximum are higher) for increased thickness of alumina layers. The work of fracture of samples is inversely proportional to the thickness and, consequently, to the volume of pure alumina. The presence of residual stresses, even in low values, might have affected the fracture behavior of composites.

ACKNOWLEDGMENTS

This work was conducted during an internship supported by the International Cooperation Program PROBRAL at the Hamburg University of Technology, which was financed by CAPES – Brazilian Federal Agency for Support and Evaluation of Graduate Education within the Ministry of Education of Brazil, and DAAD – German Academic Exchange Service. The experimental work at TUHH was partly funded by the Deutsche Forschungsgemeinschaft (DFG, German Research Foundation) – Project number 192346071 – SFB 986 (project C5). Open access funding enabled and organized by Projekt DEAL.

ORCID

Marcelo Daniel Barros https://orcid.org/0000-0002-6105-5828
Hans Jelitto https://orcid.org/0000-0002-2285-9989
Dachamir Hotza https://orcid.org/0000-0002-7086-3085
Rolf Janssen https://orcid.org/0000-0001-7054-0510

REFERENCES

1. Clegg WJ, Kendall K, Alford NM, Button TW, Birchall JD. A simple way to make tough ceramics. Nature. 1990;347(6292):455–7.
2. Bueno S, Baudín C. Design and processing of a ceramic laminate with high toughness and strong interfaces. Compos Part A Appl Sci Manuf. 2009;40(2):137–43.
3. Chlup Z, Hadraba H, Slabáková L, Drdlík D, Dlouhý I. Fracture behaviour of alumina and zirconia thin layered laminate. J Eur Ceram Soc. 2012;32(9):2057–61.
4. Barros MD, Rachadel PL, Fredel MC, Janßen R, Hotza D. Mechanical behaviour of zirconia-toughened alumina laminates with or without Y-PSZ intermediate layers. J Ceram Sci Technol. 2018;09(1):69–78.
5. Chang Y, Bermejo R, Ševeček O, Messing GL. Design of alumina-zirconia composites with spatially tailored strength and toughness. J Eur Ceram Soc. 2015;35(2):631–40.
6. Bermejo R, Danzer R. High failure resistance layered ceramics using crack bifurcation and interface delamination as reinforcement mechanisms. Eng Fract Mech. 2010;77(11):2126–35.
7. Lube T, Pascual J, Chalvet F, de Portu G. Effective fracture toughness in Al_2O_3-Al_2O_3/ZrO_2 laminates. J Eur Ceram Soc. 2007;27(2–3):1449–53.

8. Sánchez-Herencia AJ, Baudín C. Ceramic laminates with tailored residual stresses. Bol Soc Espanõla Cerámica y Vidr. 2009;48(6):311–20.
9. de Portu G, Micele L, Pezzotti G. Laminated ceramic structures from oxide systems. Compos Part B Eng. 2006;37(6):556–67.
10. Blaese D, Benitez T, Barros MD, Jelitto H, Travitzky N, Hotza D, et al. R-curve behavior and flexural strength of zirconia-toughened alumina and partially stabilized zirconia composite laminates. Ceram Int. 2018;44(12):13463–8.
11. Kübler J, Blugan G, Jelitto H, Schneider GA, Dobedoe R. Structural micro-layered ceramics with surfaces under tension and compression with increasing apparent fracture toughness. Key Eng Mater. 2007;336:2564–8.
12. Pontin MG, Lange FF. Effects of porosity on the threshold strength of laminar ceramics. J Am Ceram Soc. 2005;88(2):376–82.
13. Sørensen BF, Horsewell A. Crack growth along interfaces in porous ceramic layers. J Am Ceram Soc. 2004;84(9):2051–9.
14. Davis JB, Kristoffersson A, Carlström E, Clegg WJ. Fabrication and crack deflection in ceramic laminates with porous interlayers. J Am Ceram Soc. 2000;83(10):2369–74.
15. Clegg WJ. The fabrication and failure of laminar ceramic composites. Acta Metall Mater. 1992;40(11):3085–93.
16. Blanks KS, Kristoffersson A, Carlström E, Clegg WJ. Crack deflection in ceramic laminates using porous interlayers. J Eur Ceram Soc. 1998;18(13):1945–51.
17. Sglavo VM, Bellettati N. Ceramic laminates with improved mechanical reliability by tailoring the porosity of the constituting layers. J Eur Ceram Soc. 2017;37(4):1643–50.
18. Ma J, Wang H, Weng L, Tan GEB. Effect of porous interlayers on crack deflection in ceramic laminates. J Eur Ceram Soc. 2004;24(5):825–31.
19. Bueno S, Baudín C. Layered materials with high strength and flaw tolerance based on alumina and aluminium titanate. J Eur Ceram Soc. 2007;27(2–3):1455–62.
20. Kothari NC. The effect of particle size on sintering kinetics in alumina powder. J Nucl Mater. 1965;17(1):43–53.
21. Fang ZZ, Wang H. Densification and grain growth during sintering of nanosized particles. Int Mater Rev. 2008;53(6):326–52.
22. Winkler ER, Sarver JF, Cutler IB. Solid solution of titanium dioxide on aluminum oxide. J Am Ceram Soc. 1945;49(12):634–7.
23. Cutler IB, Bradshaw C, Christensen CJ, Hyatt EP. Sintering of alumina at temperatures of 1400°C and below. J Am Ceram Soc. 1957;40(4):134–9.
24. Jones JT, Maitra PK, Cutler IB. Role of structural defects in the sintering of alumina and magnesia. J Am Ceram Soc. 1958;41(9):353–7.
25. Kostic E, Kiss SJ, Boskovic S. Sintering and microstructure development in the Al2O3-MnO-TiO2 system. Powder Metall Int. 1990;22(2):29–30.
26. Xue LA, Chen IW. Low-temperature sintering of alumina with liquid-forming additives. J Am Ceram Soc. 1991;74(8):2011–3.
27. Sathiyakumar M, Gnanam FD. Influence of MnO and TiO_2 additives on density, microstructure and mechanical properties of Al_2O_3. Ceram Int. 2002;28(2):195–200.
28. Casellas D, Ràfols I, Llanes L, Anglada M. Fracture toughness of zirconia-alumina composites. Int J Refract Met Hard Mater. 1999;17(1):11–20.
29. Moon RJ, Bowman K, Trumble K, Rödel J. Comparison of R-curves from single-edge V-notched-beam (SEVNB) and surface-crack-in-flexure (SCF) fracture-toughness test methods on multilayered alumina – Zirconia Composites. J Am Ceram Soc. 2000;83(2):445–7.
30. Jelitto H, Hackbarth F, Özcoban H, Schneider GA. Automated control of stable crack growth for R-curve measurements in brittle materials. Exp Mech. 2013;53(2):163–70.
31. Özcoban H, Jelitto H, Schneider GA. Influence of finite notch root radius and optically determined crack length on the measured fracture toughness of brittle materials. J Eur Ceram Soc. 2010;30(7):1579–83.
32. Fett T, Fünfschilling S, Hoffmann MJ, Oberacker R, Jelitto H, Schneider GA. R-curve determination for the initial stage of crack extension in Si3N4. J Am Ceram Soc. 2008;91(11):3638–42.
33. Chartier T, Merle D, Besson JL. Laminar ceramic composites. J Eur Ceram Soc. 1995;15(2):101–7.
34. Oliver WC, Pharr GM. Measurement of hardness and elastic modulus by instrumented indentation: advances in understanding and refinements to methodology. J Mater Res. 2004;19(1):3–20.
35. Jelitto H, Felten F, Häusler C, Kessler H, Balke H, Schneider GA. Measurement of energy release rates for cracks in PZT under electromechanical loads. J Eur Ceram Soc. 2005;25(12):2817–20.
36. Fett T, Diegele E. Indirect measurements of compliance in four-point-bending tests. J Test Eval. 1988;16(5):487–8.
37. Munz D, Fett T. Ceramics: mechanical properties, failure behaviour, materials selection. Berlin: Springer; 1999.
38. Sathiyakumar M, Gnanam FD. Influence of additives on density, microstructure and mechanical properties of alumina. J Mater Process Technol. 2003;133(3):282–6.
39. Erkalfa H, Misirli Z, Baykara T. Densification of alumina at 1250 °C with MnO2 and TiO2 additives. Ceram Int. 1995;21(5):345–8.
40. Bagley RD, Cutler IB, Johnson DL. Effect of TiO_2 on initial sintering of Al_2O_3. J Am Ceram Soc. 1970;53(3):136–41.
41. Sōmiya S, editor. Handbook of advanced ceramics: materials, applications, processing, and properties. London: Academic Press; 2013.
42. Wachtman JB, Cannon WR, Matthewson MJ. Mechanical properties of ceramics. New York: Wiley; 2009.
43. Neumann M, Gehre P, Kübler J, Dadivanyan N, Jelitto H, Schneider GA, et al. Stable crack propagation in free standing thermal sprayed Al_2O_3 and Al_2O_3-ZrO_2-TiO_2 coatings. Ceram Int. 2019;45(7):8761–6.
44. He M, Hutchinson JW. Crack deflection at an interface between dissimilar elastic materials. Int J Solids Struct. 1989;25(9):1053–67.

How to cite this article: Daniel Barros M, Jelitto H, Hotza D, Janssen R. Microstructure and mechanical behavior of TiO_2-MnO-doped alumina/alumina laminates. *J Am Ceram Soc*. 2021;104:1047–1057. https://doi.org/10.1111/jace.17490